Rev. Roum. Sci. Techn.– Électrotechn. et Énerg.
Vol. **71**, *2*, pp. 187–194, Bucarest, 2026

THREE-END TRAVELING WAVE FAULT LOCATION BASED ON ELECTROMAGNETIC DECOUPLING

NURADEEN AISAR[1,2], RUIKUN MAI[1], LING FU[1]

Keywords: Three-end; Wave velocity; Time of arrival; Fault location; Transmission lines.

This study introduces a novel three-end traveling-wave-based fault location (TW-FL) method for transmission lines to improve fault location accuracy and speed. Unlike traditional approaches, it eliminates the need for traveling-wave velocity and line-parameter measurements by analyzing current surges at three terminals and exploiting the time-of-arrival (TOA) of fault-induced waves to compute the fault location. For validation, the velocity implicitly derived from the TOA formulation was compared with its theoretical value, achieving an estimation accuracy of up to 99.96%, confirming the internal consistency and robustness. The model attained maximum and minimum fault location errors of 0.36% and 0.0803%, respectively, over 100 km from terminal P, demonstrating superior accuracy relative to existing models. Simulations conducted in PSCAD/EMTDC under various fault conditions verified its robustness, while validation of the WSCC 9-bus system confirmed its speed and reliability in improving grid performance and reducing power outage.

1. INTRODUCTION

Power transmission lines, which are composed of high-voltage conductors, are supported by towers or poles [1,2] and play a critical role in ensuring reliable electricity delivery [3]. Faults in transmission systems disturb the steady-state operating conditions and interrupt power delivery, thereby necessitating precise fault location (FL) to ensure effective protection coordination and minimize outage duration [4,33]. Existing FL techniques can be broadly classified into impedance-based (Z-based) [5,6] and traveling-wave-based (TW-based) methods [6,7], while intelligence and online-based are presented in [8,9] among others. Impedance-based approaches are widely adopted in practice; however, their accuracy is significantly affected by line parameter uncertainties, load variations, and fault-arc impedance. Although two-end Z-based methods have been proposed to enhance accuracy, their performance is often limited by the synchronization requirements and communication delays. In contrast, TW-based methods exploit high-frequency fault-generated transient signals and are less dependent on steady-state system parameters than other methods. Early TW-based studies primarily employed a single-end analysis using wave time-of-arrival (TOA) information [10]. However, their accuracy is adversely affected by noise, signal attenuation, and wave dispersion. To overcome these limitations, two-end TW-based methods have been introduced, which improve the FL accuracy by comparing the TOA recorded at both terminals [11–16]. Recently, high-speed current traveling wave (CTW) measurements combined with advanced filtering techniques have been investigated to mitigate the challenges associated with voltage-based measurements, as presented in [17,18,36]. Nevertheless, these methods still require precise time synchronization, and their performance is sensitive to errors in wave velocity (WV) estimation. In addition, the need for backup protection schemes is a practical concern.

To address these shortcomings, advanced algorithms incorporating pilot impedance methods and time-synchronized measurements have been introduced to enhance sensitivity and improve FL precision. [19,20] [pp. 161–187,21]. These approaches employ the continuous wavelet transform (CWT) to extract the TW from fault signals and mitigate synchronization-related problems. In [22], an alternative method introduced an artificial fault for estimating the WV. However, this approach is invasive and may not be suitable for practical use. Other methods that do not require midline measurements to identify incidents and reflect TW-TOAs at a single measurement point have also been reported in [23,25], although the reliable discrimination of the reflected waves remains challenging. Furthermore, multi-terminal TW-FL techniques that incorporate frequency-dependent transmission line models and distance matrix formulations, which require synchronized measurements from multiple terminals, are presented in [24], thereby increasing the communication requirements, computational burden, and overall system complexity. Recent studies [26–28] have introduced enhanced analytical and protection strategies for transmission systems, focusing on improving the FL accuracy, computational efficiency, and robustness under dynamic and transient operating conditions. For instance, [27] specifically investigated the FL in wind turbine-integrated transmission networks and demonstrated improved performance through simulation-based validation. Although these approaches achieve measurable improvements over conventional Z-based techniques, they primarily rely on steady-state or phasor-domain analyses and do not fully address the challenges associated with high-frequency TW phenomena, such as precise TOA detection and wave propagation uncertainties. Consequently, the development of accurate and time-efficient TW-based FL methods is essential for enhancing power system reliability, reducing maintenance efforts, and minimizing the duration of outages. In this study, a three-end TW-FL method is presented to address some limitations associated with conventional two-end approaches. The proposed approach examines fault-induced traveling wave components captured at the three terminals of a three-terminal transmission line and incorporates electromagnetic decoupling to suppress modal coupling effects, thereby enhancing FL precision and minimizing ambiguity. Unlike several existing techniques, the proposed approach does not rely on prior knowledge of the WV, which enhances its suitability for scenarios involving limited terminal accessibility and complex network configurations. Although the study assumes generally consistent electromagnetic characteristics along the line, the developed algorithm accounts for variations in the TW behavior, contributing to

---

[1] School of Electrical Engineering, Southwest Jiaotong University, Chengdu, China.
[2] Department of Electrical/Electronics, FCE (T) Bichi, Kano State, Nigeria.
Emails: aisarnuradeen@my.swjtu.edu.cn, mairk@swjtu.edu.cn, lingfu@swjtu.edu.cn

DOI: 10.59277/RRST-EE.2026.2.3

robust performance under practical operating conditions.

2. TRAVELING WAVES ANALYSIS

2.1 ANALYSIS OF ELECTROMAGNETIC PHENOMENA

The TW-FL methods are particularly suited for long TL, where fault-induced voltage and current disturbances propagate as TW. These methods exploit the propagation characteristics of such waves to determine the FL and require a minimum wavefront magnitude for the reliable operation of the system. To facilitate the analytical formulation, Fig. 1 shows the three-terminal TL configuration used in this study, and Fig. 2 shows the fully transposed TL model adopted for the TW analysis. However, in practical power systems, three-phase faults introduce electromagnetic coupling among phases and between the phases and ground, which must be appropriately decoupled to achieve an accurate FL. Accordingly, the voltage and current along the fully transposed line are analyzed as functions of both position and time [20, pp. 161].

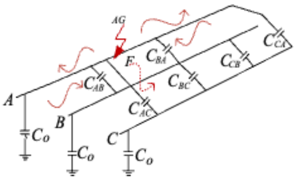

Fig 1 – Electromagnetic phenomena on three phases during faults.

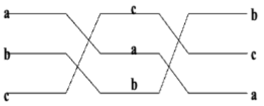

Fig. 2. Fully transposed 3Φ lines.

Figure 1 provides the basis for deriving eq. (1)–(7) for the inductance (L) and capacitance (C) under fault conditions. The mathematical formulation of the TL capacitance is provided in (1)–(4), as follows:

$$-\frac{\partial i_{\mathrm{A}}}{\partial x}=(C_{Ax}+C_{AB}+C_{AC})\frac{\partial u_A}{\partial t}-C_{AB}\frac{\partial u_B}{\partial t}-C_{AC}\frac{\partial u_C}{\partial t}. \qquad (1)$$

But $C_{AB}=C_{AC}=C_m$

$$-\frac{\partial i_{\mathrm{A}}}{\partial x}=(C_{Ax}+2C_m)\frac{\partial u_A}{\partial t}-C_m\frac{\partial u_B}{\partial t}-C_m\frac{\partial u_C}{\partial t}. \qquad (2)$$

Similarly,

$$-\frac{\partial i_{\mathrm{B}}}{\partial x}=-C_m\frac{\partial u_A}{\partial t}(C_{Bx}+2\,C_m)\frac{\partial u_B}{\partial t}-C_m\frac{\partial u_C}{\partial t}, \qquad (3)$$

$$-\frac{\partial i_{\mathrm{C}}}{\partial x}=-C_m\frac{\partial u_A}{\partial t}-C_m\frac{\partial u_B}{\partial t}+(C_{Cx}+2C_m)\frac{\partial u_C}{\partial t}, \qquad (4)$$

where C_{Ax},C_{Bx} and C_{Cx} are the capacitances of each phase to ground, C_m is the mutual capacitance between the phases, measured in Farad per meter (F/m), while U_A, U_B, U_C are the line voltages in kV.

2.1.1 LINE INDUCTANCE

To determine the inductance of an individual conductor in a 3Φ, an equal spacing between the conductors is assumed, that is $d_1 = d_2 = d_3$, and the currents are, respectively I_a , I_b, and I_c. As shown in eq. (1)–(4), the total capacitance is the sum of the self and mutual inductances of each conductor. The equations for the inductance of the line are presented in (5)–(7).

$$L_A=\left\{2\mathrm{Log_e}\ \frac{d}{r}+\frac{1}{2}-2(-0.5+\mathrm{j}0.866)\mathrm{Log_e}\ 2\right\}\times 10^{-7}\ \text{H/m} \ (5)$$

$$L_B=\left\{2\mathrm{Log_e}\ \frac{d}{r}+\frac{1}{2}\right\}\times 10^{-7}\ \text{H/m} \qquad (6)$$

$$L_C=\left\{2\mathrm{Log_e}\ \frac{d}{r}+\frac{1}{2}-2(-0.5\text{-}\mathrm{j}0.866)\mathrm{Log_e}\ 2\right\}\times 10^{-7}\ \text{H/m} \qquad (7)$$

where L_A, L_{B} and L_{C} are the lines inductances measured in H/m, d is the line spacing (m), and r is the radius of the conductor (m).

It should be noted that in extra-high-voltage transmission lines (EHV-TLs), the corona discharge becomes more significant. The use of bundle conductors can reduce this effect by decreasing line reactance and power losses.

2.1.2 LINE CAPACITANCE

The capacitance (C) between parallel conductors depends on their size and spacing. For short lines (≤ 80 km), the capacitance effect is negligible. However, for a long HVTL, the capacitance and the charging currents become significant, even when the line is open. Although the voltage varies between conductor sections, the average voltage can be determined. Using this average voltage, the line capacitance can also be determined as shown in eq. (8) [20 (pp. 161–187)].

$$V_{AB}=\frac{1}{2\pi k}\left(q_{\mathrm{A}}\ln\frac{D_{eq}}{r}+\mathrm{q_B}\ln\frac{\mathrm{r}}{\mathrm{D_{eq}}}\right)[V], \qquad (8)$$

where V_{AB} represents the potential difference between conductors A and B measured in kilovolts. $D_{eq} = \sqrt[3]{D_{AB}D_{BC}D_{AC}}$, r [m] is the radius of the conductor, and D_{ij} [m] is the distance between line i and line j of the TL, q_{A}, q_{B} and q_C and are the charge per unit length on conductor A, B, and C. The linear charge density q is measured in [C/m]. Similarly.

$$V_{AC}=\frac{1}{2\pi\mathrm{k}}\left(\mathrm{q_A}\ln\frac{\mathrm{D_{eq}}}{\mathrm{r}}+\mathrm{q_C}\ln\frac{\mathrm{r}}{\mathrm{D_{eq}}}\right)[\mathrm{V}], \qquad (9)$$

where V_{AC} represents the potential difference between conductors A and C measured in kilovolts. Generally, the capacitance to neutral for a single three-phase circuit is represented by

$$C_n=\frac{2\pi k}{\ln\left(\frac{D_{eq}}{D_{SC}}\right)}\ \text{F/m to neutral,} \qquad (10)$$

where D_{SC} is the external radius of the conductor (m), k is an electrical constant. For an overhead line $k = 8.84 \times 10^{-12}$ F/m, and for air $k_r = 1.00054$. Hence, the equivalent matrices for **C** and **L** are expressed as

$$\mathbf{C}=\begin{bmatrix}(C_{Ax}+2C_m) & -C_m & -C_{0_{\mathrm{m}}}\\ -C_m & (C_{Bx}+2C_m) & -C_m\\ -C_m & -C_m & (C_{Cx}+2C_m)\end{bmatrix} \text{ and } \mathbf{L}=\begin{bmatrix}L_s & L_m & L_m\\ L_m & L_s & L_m\\ L_m & L_m & L_s\end{bmatrix} \qquad (11)$$

where L_s and L_m are the line self and mutual inductance, respectively.

2.2 PHASE TO MODAL TRANSFORMATION

Clarke's transformation simplifies the analysis of 3Φ TL by converting the currents of each phase (a, b, c) into a new two-dimensional space with alpha (α) and beta (β) components. This reduces complex calculations while focusing on the overall power flow in the system, making it an important tool for balanced 3Φ analysis [2,13]. Equation (12) shows a simplified version of Clarke's transformation.

$$\begin{bmatrix}I_0\\ I_\alpha\\ I_\beta\end{bmatrix}=\frac{1}{3}\begin{bmatrix}1 & 1 & 1\\ 2 & -1 & -1\\ 0 & \sqrt{3} & -\sqrt{3}\end{bmatrix}\begin{bmatrix}\mathrm{I_A}\\ I_B\\ I_C\end{bmatrix} \qquad (12)$$

where I_0,I_α and I_β are the ground mode and the two aerial modes, respectively. I_0 denotes the ground mode signal, which is due to the earth's losses, possesses more attenuation than the aerial mode. Whereas the α mode is suitable for the analysis of TWs launched by line-to-ground (L-G) faults, the β component is more suitable for the analysis of TWs launched by line-to-line (L-L) faults. The first and second aerial modes have impedances like the positive and negative sequence impedances of the line. This is because the LPs are the same for positive or negative sequence faults.

2.3 REFLECTIONS AND REFRACTIONS

Traveling EMW on TL has a fixed voltage-current (V-I) relationship when the characteristic impedance remains constant. Faults, such as short circuits, cause partial wave reflection. V and I waves remain continuous at this fault point, and the total wave energy is conserved. The behavior of the reflected V and I waves can be quantified using the reflection coefficient, $\zeta = 2k/k+1$ and $\gamma = k\text{-}1/k+1$ is the reflection coefficient. Where, $k = Z_1/Z_2$, Z_1 is the wave impedance of the incident wave (measured in ohms), and Z_2 is the equivalent impedance at the point J in the incident wave direction (refers to Figs. 3 and 4). In power TL, especially during faults, understanding the behavior of EM waves on TL is crucial.

2.3.1 INCIDENT WAVE CALCULATIONS

Consider a wave of electrical energy traveling along a healthy TL. This initial wave, carrying V and I, is called the incident wave. As long as the line remains intact, this wave propagates towards its destination if there is no other interruption. Equations (13) and (14) represent the incidence and reflected wave equations for V and I, respectively [19,21,24 (pp. 234–235)].

$$i_f = \sqrt{\frac{C}{L}}\exp\text{-}(R/L)t f_1\left(t\text{-}\frac{x}{v}\right), \tag{13}$$

$$r_f = \exp\text{-}(R/L)t f_2\left(t\text{-}\frac{x}{v}\right). \tag{14}$$

2.3.2 REFLECTED WAVE CALCULATIONS

When a fault occurs on a TL, it disrupts the TL impedance. This causes part of the incoming wave to be reflected. The V and I of the reflected wave can also be determined from

$$i_f = \text{-}\sqrt{\frac{C}{L}}\exp\text{-}(R/L)t f_1\left(t+\frac{x}{v}\right), \tag{15}$$

$$r_f = \exp\text{-}(R/L)t f_2\left(t+\frac{x}{v}\right), \tag{16}$$

where f_1 and f_2 are the functions of the incident and reflected waves, respectively; x is the distance (m); and R is the resistance (Ω) of the line. In the above equations, the functions f_1 and f_2 must be single-valued to accurately determine the FL.

3. PROPOSED THREE-END METHOD

Connection points added to existing power lines, rather than new lines, meet the increased power demands [29–32]. This study proposes a three-end TW-based FL technique that improves the accuracy of two-end methods. By analyzing the TWs at three points and comparing the arrival time differences, the method accurately pinpoints the FL, particularly for LTLs.

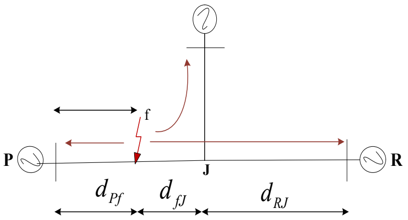

Fig. 3. Simplified circuit for the three-end method.

Figure 3 illustrates the simplified circuit used in the proposed method. When a fault occurs along PJ, TWs arrive at points P, Q, and R sequentially, with the TOA varying according to the distance, and the TOA propagation is as shown in Fig. 4. Although the order of arrival at Q and R is inconsequential, a precise TOA analysis at all three points is vital. Point P receives multiple reflected waves, complicating the FL and highlighting the limitations of Bewley's lattice diagram, which can produce misleading results in certain cases.

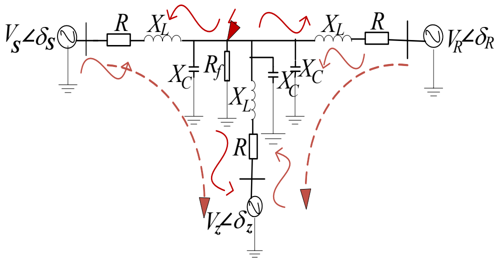

Fig. 4 – Traveling wave paths of a three-end network.

3.1 FAULT SECTION IDENTIFICATION (FSI) LOGIC

In this method, to determine the FSI, a detailed breakdown of each condition is provided by the following eq. (17)–(20).

1. If the TOA reaches P before R and Q, then the fault is likely to be on the PJ section, as shown in Fig. 6(a).

$$\tau_Q > \tau_P < \tau_R \text{ ; for } 0 < d < 1/2 \tag{17}$$

2. If the TOA reaches R first before P and Q, then the fault is likely on the RJ of the line, as shown in Fig. 6(b).

$$\tau_P > \tau_R < \tau_Q \text{ ; for } 1/2 < d \leq 1 \tag{18}$$

3. If the TOA at P and R are equal, the fault may be at the J, and JQ contains the real fault, as shown in Fig. 6©.

$$(\tau_P = \tau_R) < \tau_Q \text{ ; for } d = 1/2 \tag{19}$$

4. If a fault occurs at JQ section, point Q receives the real fault information first; for a fault within JQ section, see Fig. 6(d),

$$\tau_P > \tau_Q < \tau_R \text{ ;.} \tag{20}$$

where τ_P , τ_Q, and τ_R are the TOA at points P, Q, and R, respectively.

3.2 FAULT LOCATION ESTABLISHMENT

Consider a T-shaped three-end LTL, as shown in Fig. 3, with the assumption that point J is the middle of the TL connecting P, Q, and R. The fault locators were positioned at P, Q, and R, where current measurements were performed. For a fault occurring along the PJ of line PR, as shown in Fig. 6(a), eq. (21) can be used for an accurate FL,

$$D_{PQ} = \frac{\left(\tau_{P_2}\text{-}\tau_{P_1}\right)l_{PQ}}{2\tau_{Q_1}+\left(2\tau_{P_2}\text{-}4\tau_{P_1}\right)} \text{ km}, \tag{21}$$

For the fault that occurs along the RJ of line PR, as shown in Fig. 6(b), eq. (22) is used to compute the FL,

$$D_{RQ} = \frac{\left(\tau_{R_2}\text{-}3\tau_{R_1}+2\tau_{Q_1}\right)l_{RQ}}{2\left(\tau_{R_2}+\tau_{Q_1}\right)\text{-}4\tau_{R_1}} \text{ km}. \tag{22}$$

For the fault that occurred along QJ of line PR, as shown in Fig. 6(c). A classical single-end can be used to detect FL accurately using eq. (23), as line QJ is the only line containing the real fault. Thus,

$$d_{Qf} = \frac{\left(\tau_{Q_2}\text{-}\tau_{Q_1}\right)}{2} v_{lp} \text{ km}, \tag{23}$$

where v_{lp} is the line WV. Similarly, for the FL at the J point, as shown in Fig. 6(d), PR with J as the midpoint of the line connecting Q at J. Thus, eq. (24) can be used for accurate FL.

$$d_C = \frac{\left(\begin{matrix}\tau_{P_1}{}^2+\tau_{R_1}{}^2\text{-}\tau_{P_1}\tau_{P_2}\text{-}4\tau_{P_1}\tau_{R_1}+3\tau_{P_1}\tau_{R_2}\\ +3\tau_{P_2}\tau_{R_1}\text{-}2\tau_{P_2}\tau_{R_2}\text{-}\tau_{R_1}\tau_{R_2}\end{matrix}\right)l_{PR}}{4\left(2\tau_{P_1}\text{-}\tau_{P_2}\text{-}\tau_{R_1}\right)\left(\tau_{P_1}\text{-}2\tau_{R_1}+\tau_{R_2}\right)} \text{ km} \tag{24}$$

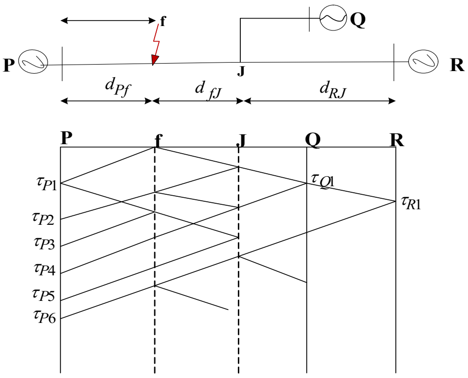

Fig. 5 – Bewley Lattice Diagram for a fault occurring at PJ.

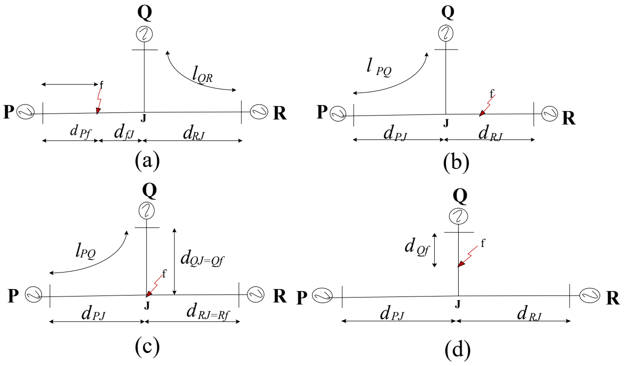

Fig. 6 – Fault cases at different sections of the line.

3.3 OVERALL FLOWCHART OF THE PROPOSED THREE-END TW-FL ALGORITHM

To enhance clarity, a step-by-step overview of the proposed three-end TW-FL algorithm, and a flowchart illustrating the complete processing sequence are presented in Fig. 7.

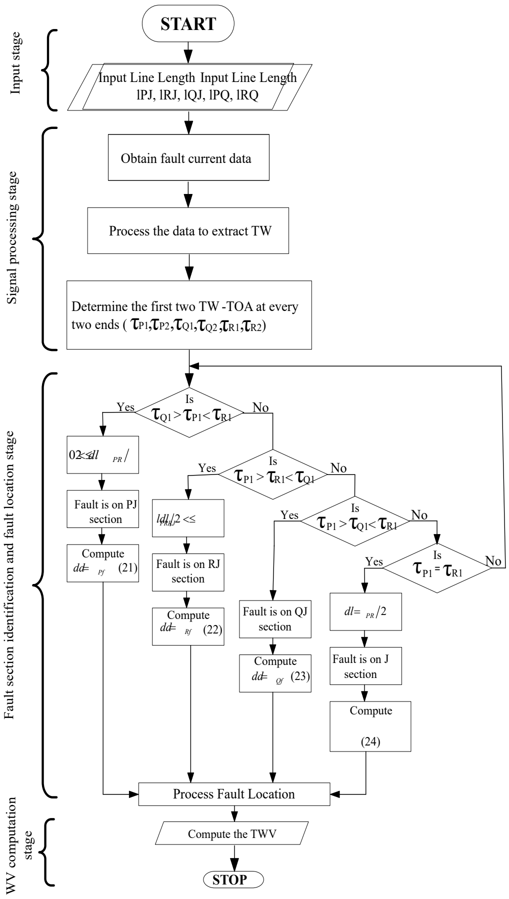

Fig. 7 – Flowchart representation of the proposed fault location algorithm.

The flowchart summarizes the major stages of the method, including input data specification, fault current acquisition, TW extraction, TOA determination, FS identification, fault distance computation, and WV estimation. This graphical representation is intended to complement the mathematical formulation by clearly illustrating the logical decision process and the steps involved in the proposed scheme.

4. ILLUSTRATIVE EXAMPLE

A PSCAD/EMTDC simulation analyzed a 400 kV, 50 Hz TL, 300 km from P to R. At 150 km, a 50 km branch line was tapped. Assuming a ground resistivity of 100 Ω-m, the fault locators were installed at P, Q, and R. The simulation incorporated CTs and CVTs for precise V and I measurement. In this study, we focused on the fault current signal from the CT owing to its high-frequency response for the TW-FL [15]. Measurements were taken at 1 MHz, and the sampling frequency was selected such that the sample of the signals was taken at the Nyquist value to prevent aliasing and at a threshold of 2 µs. Finally, the FL percentage error is determined using Equation (25).

$$E = \left| \frac{\text{AFL-EFL}}{\text{TLL}} \right| \times 100\% \qquad (25)$$

where e is the fault location percentage error (%). AFL and EFL are the actual fault location (km) and estimated fault location (km), respectively, whereas TLL is the Total Line Length (km).

5. RESULTS ANALYSIS AND DISCUSSIONS

This section evaluates the performance and accuracy of the proposed method. Specifically, the following analysis examines its capability to identify and accurately locate faults within power systems (PS). Table 1 presents a comparison of the FL results obtained using the single-end (SE) and two-end (TE) schemes across different line sections.

Table 1

Test results indicate a fault at QJ.

FL Type	SE_{QP}	TE_{QP}	SE_{QJ}	TE_{QJ}	SE_{QR}	TE_{QR}
FL	169.203	171.63	30.797	28.37	169.204	171.63
FLE (%)	0.00399	0.00815	0.01594	0.0326	0.00399	0.00815
FLE (m)	7.98	16.30	7.97	16.30	7.98	16.30

Both approaches provided reasonably accurate FL estimates; however, the SE scheme exhibited consistently lower FLE values than the TE scheme in all the evaluated cases. The absolute errors for the SE method remained within approximately 8 m, whereas those for the TE method were approximately 16 m. These results indicate that the SE approach offers improved precision under the considered scenarios, specifically in the tapped line in the proposed method, whereas the TE method continues to provide acceptable performance.

Table 2 summarizes the TW-TOA measurements at terminals P, Q, and R, along with the corresponding estimated FL and FLEs for various fault positions along the three-terminal TL. The results demonstrate that the proposed method accurately identifies FL across a wide range of scenarios, including faults near individual terminals and within shared line sections. The estimated locations closely matched the actual fault positions in most cases, with small relative errors and meter-level absolute errors achieved at a sampling frequency of 1 MHz. Variations in accuracy were observed with respect to the fault proximity to the measuring terminals, which is consistent with the TW attenuation and dispersion characteristics. Overall, the results confirm the robustness and practical applicability of the proposed three-end approach for multiterminal transmission systems.

Table 2

Test results for the proposed fault location method.

Fault TOA/ Parameter	FL at 20km from P	FL at 50km from P	FL at 90km from P	FL at 100km from P	FL at 150km from P&R	FL at 30km from Q	FL at 160km from R
τ_{P_1} (μs)	69	170	308	345	518	624	825
τ_{P_2} (μs)	206	516	928	1035	1550	1860	1377
τ_{Q_1} (μs)	620	519	378	350	173	106	138
τ_{Q_2} (μs)	1032	840	998	1040	517	310	413
τ_{R_1} (μs)	966	595	719	689	518	625	550
τ_{R_2} (μs)	2884	1850	2165	2070	1549	1861	918
d_P (km)	19.912	49.78	89.8	99.28	150.00	169.203	159.447
d_Q (km)	177.218	150.089	110.144	100.71	NA	30.797	40.029
d_R (km)	280.502	249.807	209.565	199.759	150.00	169.204	160.8
FLE_P (%)	0.044	0.11	0.10	0.36	0.00	0.399	0.276
FLE_Q (%)	1.391	0.089	0.072	0.355	NA	0.399	0.0145
FLE_R (%)	1.673	0.064	0.145	0.0803	0.00	0.398	0.40
FLE_P (m)	88	220	200	720	0.00	797	553
FLE_Q (m)	13.91	89	144	710	NA	797	800
FLE_R (m)	502	193	435	241	0.00	796	720

5.1 COMPARATIVE PERFORMANCE ANALYSIS WITH OTHER FAULT LOCATION ALGORITHMS

To assess the effectiveness of the proposed method, a fault 20 km from P was simulated.

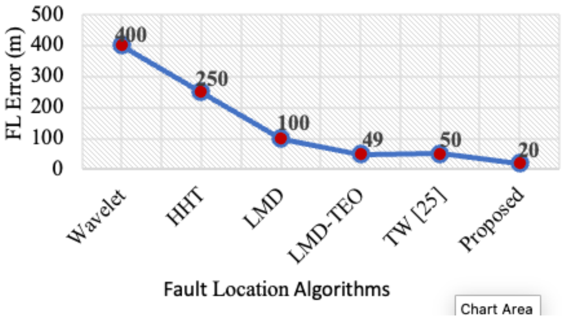

Fig. 8 – Comparison with other fault location algorithms.

The comparative results are shown in Fig. 8, which shows that the proposed method performs better in FL than the classical methods. The results were then compared with those obtained from other established FL techniques, including wavelet (db3), Hilbert-Huang transform (HHT), local mean decomposition (LMD), LMD Teager energy operator (LMD-TEO), and a TW-based method [25].

5.2 COMPARISON WITH OTHER WAVE VELOCITY CALCULATION TECHNIQUES

This section presents a comparative analysis between the proposed method and classical approaches that rely on either the measured or estimated WV.

As shown in Table 3, the method reported in [31] determined the WV as 298.507 km/ms, whereas the approach in [26] employed an empirically estimated value of 299.710 km/ms for the TW. In contrast, the WV estimated using the proposed method was 299.790 km/ms (Table 3), indicating improved accuracy. In addition, the proposed approach does not require comprehensive knowledge of line parameters, auxiliary line energization procedures, or empirically derived estimates because it relies solely on TW-TOA information.

Table 3

Comparative analysis with existing multi-terminal fault location techniques.

Algorithm	[30]	[32]	[31]	[29]	[26]	[Proposed]
Max error (m)	3360	380	129	1280	69	800
Measurement	Voltage	Voltage	Current	Voltage	Voltage	Current
f_s (kHz)	10	40	2000	200	1000	1000
Methods	Impedance	AI	TW	TW	TW	TW
FSI	Yes/Complex	Yes/Complex	Yes/Complex	Yes/Complex	Yes/Complex	No/Simple Logic
TWV Estimation ($\text{x}10^8$m/s)	NA	NA	2.9851	NA	2.9971	2.9979

5.3 COMPARISON WITH OTHER MULTITERMINAL FAULT LOCATION METHODS

In this section, the proposed method is compared with state-of-the-art FL techniques, including impedance-based (Z-based) methods [30], artificial intelligence (AI)-based methods [32], and other TW-based approaches [31]. The comparative results are summarized in Table 3. As shown in the table, the Z-based methods require the lowest sampling frequency; however, they exhibit the lowest FL accuracy. Although AI-based methods achieve improved accuracy, they are associated with high computational complexity. Among the TW-based techniques, the method reported in [31] requires the highest sampling frequency, whereas the approach in [29] operates at a lower sampling frequency but yields a lower accuracy. In contrast, the proposed method achieves a favorable balance by providing a high FL accuracy at a practical sampling frequency of 1 MHz, which is essential for precise TW-based applications. In addition, the proposed approach demonstrates competitive computational efficiency

5.4 PERFORMANCE ON WSCC 9 BUS SYSTEM

The proposed scheme was tested and validated using the Western System Coordinating Council (WSCC) 9-bus system, a widely adopted benchmark. The system comprises three synchronous generators, six constant-parameter TL, three loads, and three two-winding transformers interconnected in a 9-bus configuration. A single-line diagram (SLD) of the system is shown in Fig. 9. Single line-to-ground (L–G) faults were introduced at distances of 20 km, 50 km, 90 km, and 100 km along different TL, with fault resistance R_f varied from 0.1 Ω to 100 Ω. Voltage and current measurements were obtained from buses 4 and 7, with each TL having a length of 200 km each. In addition, a fault with $R_f = 0.1\ \Omega$ was simulated at 100 km from bus 4 on line 4–5, and the corresponding TW-TOA signals at buses 4 and 5 were recorded. The resulting FL estimates are summarized in Table 4, and Fig. 10 illustrates the performance of the proposed method for different line sections.

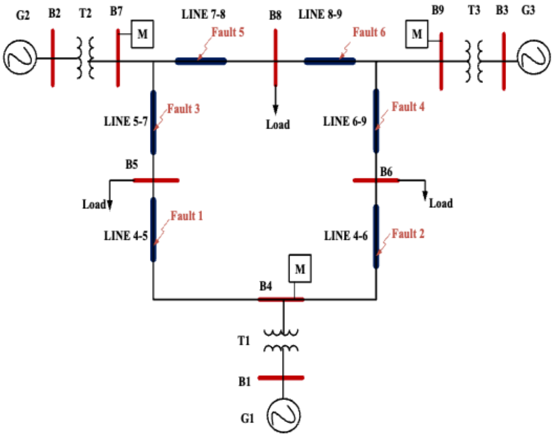

Fig. 9 – WSCC 9-bus system.

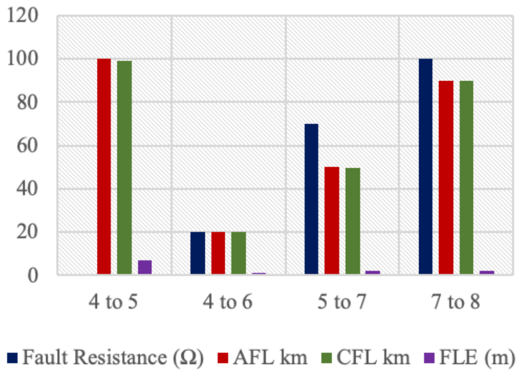

Fig. 10 – Performance on WSCC 9-bus system.

Table 4

Performance of fault location on WSCC 9-bus system.

Line section	R_f (Ω)	AFL (km)	τ_{P_1}(μs)	τ_{P_2} (μs)	τ_{Q_1} (μs)	τ_{Q_2}(μs)	CFL (km)	FLE (%)	FLE(m)
4-5	0.1	100	345	1035	350	1040	99.98	0.02	20
4-6	20	20	69	205	219	1032	19.912	0.044	88
5-7	70	50	170	516	519	840	49.78	0.11	220
7-8	100	90	308	928	378	998	89.80	0.10	200

The WSCC 9-bus system employed in this study serves as a benchmark test network to validate the feasibility and correctness of the proposed method for multiterminal TL. This validation primarily aimed to demonstrate the effectiveness of the proposed algorithmic framework using a standardized and widely used system configuration. More challenging operating conditions, including noise, time-synchronization imperfections, and complex TW reflections, were investigated through detailed simulations in which these effects could be systematically introduced and controlled. These complementary simulation studies indicate that the proposed method maintains a stable performance under nonideal conditions. Together, the benchmark validation and comprehensive simulations provide a balanced assessment of the robustness and practical applicability of the proposed method.

5.5 COMPARATIVE IMPLEMENTATION UNDER IDENTICAL CONDITIONS

To ensure a rigorous and unbiased assessment of performance, all the compared methods, including the classical approaches in [2,4,15], were implemented under strictly identical modelling and simulation conditions to ensure fairness. The same TL configuration, line parameters, fault types (LG, LL, LLL, and LLG), fault locations, fault resistances (0.1–500 Ω), fault inception angles (0°, 30°, and 60°), and sampling frequency (1 MHz) were used. Hence, the performance differences stem exclusively from the methodological formulations rather than from modeling inconsistencies. In contrast to classical methods, which involve impedance-based formulations, iterative estimation, or prior knowledge of wave velocity and detailed line parameters, the proposed approach relies on TOA estimation and direct algebraic evaluation. The elimination of iterative correction and parameter-dependent compensation reduces the computational burden, limiting processing primarily to signal detection and analytical calculation. To further clarify the quantitative and structural differences between the proposed technique and classical approaches, a concise comparative summary of fault FL and FLE is provided in Table 5.

Table 5

Comparative evaluation of accuracy, computational characteristics, and robustness under identical conditions.

Test script	Proposed Method			Classical Methods [2,4,15]	
	FIA	FL	ERROR	FL	ERROR
Type: LG	0	129.86	0.046	NA	NA
RF=0.1Ω	30	129.86	0.046	NA	NA
FL=130 km	60	129.86	0.046	NA	NA
Type: LG	0	100	0.00	99.95	0.01
RF=10 Ω	30	100	0.00	99.95	0.01
FL=100km	60	100	0.016	99.95	0.01
Type: LL	0	150	0.00	150.07	0.02
RF=100 Ω	30	150	0.00	150.07	0.02
FL=150km	60	150	0.00	150.07	0.02
Type: LL	0	250.03	0.01	250.02	0.01
RF=50 Ω	30	250.03	0.01	250.02	0.01
FL=250km	60	250.03	0.01	250.02	0.01
Type: LLL	0	49.98	0.007	49.97	0.01
RF=100 Ω	30	49.98	0.007	49.97	0.01
FL=50km	60	49.98	0.007	49.97	0.01
Type: LLG	0	126.01	1.329	NA	NA
RF=500 Ω	30	126.01	1.329	NA	NA
FL= 130km	60	125.99	1.3361	NA	NA

5.6 SENSITIVITY AND ROBUSTNESS ANALYSIS

In this section, a sensitivity analysis across wide variations in fault resistance, inception angle, fault type, and location confirmed the robustness of the model. As presented in Table 5, for LG, LL, and LLL faults, the errors remained below 0.05%, whereas even for high-resistance LLG faults of 500 Ω, the maximum deviation was approximately 1.34%, which was within acceptable protection limits. The negligible variation with the inception angle further confirms low phase sensitivity. Overall, under identical conditions, the proposed method demonstrated improved numerical stability, reduced parameter dependency, and strong resilience, thereby quantitatively supporting its advancement.

6. **CONCLUSION**

This study presents a three-end TW-FL approach for LTL, utilizing terminal measurements and electromagnetic analysis of TW propagation. By estimating the TOA at the terminals closest to the fault point, the proposed method accurately determines the FL without requiring prior knowledge of the WV or detailed line parameters of the FL. The approach was comprehensively validated through extensive PSCAD/EMTDC simulations under diverse fault types, fault resistances, fault inception angles, and fault locations, and was further evaluated using the WSCC 9-bus system. Under the investigated operating conditions and a sampling frequency of 1 MHz, the maximum FL error was limited to maximum and minimum fault location errors of 0.36% and 0.0803%, respectively, over 100 km from terminal P, thereby confirming the accuracy, robustness, and practical applicability of the proposed model for FL in LTL. Furthermore, the proposed approach can alleviate certain limitations of existing multi-terminal TW-FL techniques, particularly those related to pairwise synchronization assumptions and the neglect of electromagnetic coupling effects. By incorporating an electromagnetic decoupling framework and jointly utilizing the TW information from all three terminals, the proposed method improves fault section identification while reducing location ambiguity. Moreover, the reduced dependence on WV estimation and LP knowledge may decrease the sensitivity to parameter uncertainties. However, it should be noted that the present validation is limited to simulation-based studies; experimental verification using hardware platforms has not been addressed within the scope of this study and remains an important direction for future investigation. Overall, the findings suggest that the proposed method constitutes a practical alternative to multi-terminal TW-FL in complex transmission network configurations.

ACKNOWLEDGEMENT

This work was supported by the National Key Research and Development Program of China (2023YFB4302002).

CREDIT AUTHORSHIP CONTRIBUTION STATEMENT

NURADEEN AISAR: conceptualization; data curation; investigation; methodology; software; visualization; and writing—original draft.

RUIKUN MAI: formal analysis; investigation; resources; supervision; validation; and writing—review & editing;

LING FU: writing, review & editing.

Received April 4, 2025

REFERENCES

1. D. Wang, J. Liu, M. Hou, *Novel traveling wave fault location approach for overhead transmission lines*, International Journal of Electrical Power and Energy Systems, **155**, pp. 109617 (2024).
2. N. Aisar, R. Mai, W. Jungang, A.M. Lodha, *Enhanced and precise traveling wave fault location accuracy on transmission lines utilizing dual time of arrival*, Electrical Engineering (2024).
3. O.D. Naidu, N. George, S. Zubic, M. Krakowski, *Time-domain-based distance protection for transmission networks: secure and reliable solution for complex networks*, IEEE Access, **11**, pp. 104656–104675 (2023).
4. O.D. Naidu, A.K. Pradhan, *Precise traveling wave-based transmission line fault location method using single-ended data*, IEEE Trans. Ind. Inform., **17**, *8*, pp. 5197–5207 (2021).
5. R. Krishnathevar, E.E. Ngu, *Generalized impedance-based fault location for distribution systems*, IEEE Trans. Power Deliv., **27**, *1*, pp. 449–451 (2012).
6. R.H. Salim, K.C.O. Salim, A.S. Bretas, *Further improvements on impedance-based fault location for power distribution systems*, IET Gener. Transm. Distrib., **5**, *4*, pp. 467–478 (2011), https://digitallibrary.theiet.org/content/journals/10.1049/iet-gtd.2010.0446, accessed on 20.06.2023.
7. E.O. Schweitzer, A. Guzman, M.V. Mynam, V. Skendzic, B. Kasztenny, S. Marx, *Locating faults by the traveling waves they launch*, 2014 67th Annual Conference for Protective Relay Engineers (CPRE), pp. 95–110 (2014).
8. K. Guerraiche, A.B. Abbou, L. Dekhici, *Intelligent fault detection and location in electrical high-voltage transmission lines*, Rev. Roum. Sci. Techn. – Électrotechn. et Énerg., **69**, *3*, pp. 269–276 (2024).
9. S.D. Sessa, F. Sanniti, A. Greco, S. Talomo, M. Pajussin, R. Benato, *An online single-ended traveling waves fault detection algorithm for high-voltage multi-branch overhead lines*, IEEE Access, **12**, pp. 89691–89706 (2024).
10. D. Rezaei, M. Gholipour, F. Parvaresh, *A single-ended traveling-wave-based fault location for a hybrid transmission line using detected arrival times and TW's polarity*, Electric Power Systems Research, **210**, 108058 (2022).
11. P.O.K. Anane et al., *Traveling wave arrival time detection for two-terminal non-contact measurement based on short time matrix pencil scheme*, Electric Power Systems Research, **205**, 108165 (2022).
12. H. Lei, J. Gui, B.K. Johnson, *Impact of saturated iron core superconducting fault current limiters on traveling-wave-based protection*, IEEE Trans. Appl. Supercond., **33**, *8*, 5602305 (2023).
13. H.A. Abd El-Ghany, A.M. Azmy, A.M. Abeid, *A general traveling-wave-based scheme for locating simultaneous faults in transmission lines*, IEEE Trans. Power Deliv., **35**, *1*, pp. 130–139 (2020).
14. F. Deng et al., *A single-ended fault location method for transmission line based on full waveform features extractions of traveling waves*, IEEE Trans. Power Deliv., **38**, *4*, pp. 2585–2595 (2023).
15. O.D. Naidu, A.K. Pradhan, *Model-free traveling wave-based fault location method for series compensated transmission line*, IEEE Access, **8**, pp. 193128–193137 (2020).
16. V. Pradhan, O.D. Naidu, *Traveling wave-based setting free fault location for transmission lines using unsynchronized data*, 2023 IEEE International Conference on Energy Technologies for Future Grids (ETFG) (2023).
17. R. Liang et al., *Fault location method in power network by applying accurate information of arrival time differences of modal traveling waves*, IEEE Trans. Ind. Inform., **16**, *5*, pp. 3124–3132 (2020).
18. O.D. Naidu, S. Zubic, A.V.S.S.R. Sai, A.N. Praveen, P. Cost, H. Eriksson, *Economical setting-free double-ended fault locator for transmission lines: experiences from recent pilot installations*, IEEE Access, **10**, pp. 96805–96820 (2022).
19. M. Farshad, M. Karimi, *A signal segmentation approach to identify incident/reflected traveling waves for fault location in half-bridge MMC-HVdc grids*, IEEE Trans. Instrum. Meas., **71**, 6504111 (2022).
20. J.J. Grainger, J.W.D. Stevenson, *Power Systems Analysis*, McGraw-Hill Education, New Delhi, Chap. 5, pp. 161–187 (2015).
21. M. Davoudi, J. Sadeh, E. Kamyab, *Transient-based fault location on three-terminal and tapped transmission lines not requiring line parameters*, IEEE Trans. Power Deliv., **33**, *1*, pp. 179–188 (2018).
22. N.D. Anisimova et al., *Transient phenomena in electrical power systems problems and illustrations*, Pergamon Press, London, pp. 234–235 (1965).
23. A. Greenwood, *Electrical transients in power systems*, John Wiley & Sons, USA, Chap. 9, pp. 234–236 (1991).
24. R. Zeng, L. Zhang, Q.H. Wu, *Fault location scheme for multi-terminal transmission line based on frequency-dependent traveling wave velocity and distance matrix*, IEEE Trans. Power Deliv., **38**, *6*, pp. 3980–3990 (2023).

25. Q. Hanbo, J. Huibin, L. Hongbao, Z. Guoyun, *A traveling-wave-based fault location method in transmission line based on LMD and TEO*, Proc. International Conf. on Logistics, Engineering, Management and Computer Science (2014).
26. M. Waqas, F. Rafique, L. Fu, R. Mai, *Synthetic operational data generation for deep learning applications in power transmission lines*, Rev. Roum. Sci. Techn. – Électrotechn. et Énerg., **70**, *3*, pp. 295–300 (2025).
27. B. Ponnuswamy, C. Columbus, S.R. Lakshmi, J. Chithambaram, *Wind turbine fault modeling and classification using cuckoo-optimized modular neural networks*, Rev. Roum. Sci. Techn. – Électrotechn. et Énerg., **68**, *4*, pp. 369–374 (2023).
28. A. Saidi, D. Abdelghani, A. Touhami, *Fault detection and diagnosis in photovoltaic power systems using Fisher random matrix approach*, Rev. Roum. Sci. Techn. – Électrotechn. et Énerg., **70**, *4*, pp. 513–518 (2025).
29. Y. Zhu, X. Fan, *Fault location scheme for a multi-terminal transmission line based on current traveling waves*, International Journal of Electrical Power and Energy Systems, **53**, *1*, pp. 367–374 (2013).
30. S.M. Brahma, *Fault location scheme for a multi-terminal transmission line using synchronized voltage measurements*, IEEE Transactions on Power Delivery, **20**, *2*, pp. 1325–1331 (2005).
31. J. Ding, X. Wang, Y. Zheng, L. Li, *Distributed traveling-wave-based fault-location algorithm embedded in multiterminal transmission lines*, IEEE Transactions on Power Delivery, **33**, *6*, pp. 3045–3054 (2018).
32. B.K. Chaitanya, A. Yadav, *Decision tree aided travelling wave-based fault section identification and location scheme for multi-terminal transmission lines*, Measurement, **135**, pp. 312–322 (2019).